Numerical modeling of the optical response of supported metallic particles

Ingve Simonsen*
Laboratoire Mixte CNRS/Saint-Gobain (UMR 125) ''Surface du Verre et Interfaces,'' 39, Quai Lucien Lefranc, Boîte Postale 135, F-93303 Aubervilliers Cedex, France
and Department of Physics, Theoretical Physics Group, The Norwegian University of Science and Technology (NTNU), N-7034 Trondheim, Norway

Rémi Lazzari,† Jacques Jupille,‡ and Stéphane Roux§
Laboratoire Mixte CNRS/Saint-Gobain (UMR 125) ''Surface du Verre et Interfaces,'' 39, Quai Lucien Lefranc, Boîte Postale 135, F-93303 Aubervilliers Cedex, France
(Received 9 June 1999)

The present work reports a general method for the calculation of the polarizability of a truncated sphere on a substrate. A multipole expansion is used, where the multipoles are not necessarily localized in the center of the sphere but can freely move on the revolution axis. From the weak formulation of the boundary conditions, an infinite set of linear equations for the multipole coefficients is derived. To obtain this set, the interaction between the island and the substrate is taken into account by the technique of image multipoles. For numerical implementation, this set is truncated at an arbitrary multipole order. The accuracy of the method is judged through the stability of the truncated sphere polarizability and the fulfillment of the boundary conditions, which are demonstrated to be satisfied in large regions of the parameter space. This method brings an improvement with respect to the Bedeaux case [M. M. Wind, J. Vlieger, and D. Bedeaux, Physica A **141**, 33 (1987); M. M. Wind, P. A. Bobbert, J. Vlieger, and D. Bedeaux, *ibid* **143**, 164 (1987)] where the multipoles are located in the center of the sphere.

I. INTRODUCTION

The *in situ* characterization of the growth mode of a thin film in vacuum conditions is a long pending question. Indeed, a doubt is always shed on the *ex situ* observations of deposits, often performed by electron microscopy, which may not be representative of the studied systems during their growth. Several diffraction techniques are suited to examine the structure of the growing films. For those many techniques probing surfaces by means of charged species, such as low-energy electron diffraction and reflection high-energy electron diffraction, the charge buildup prevents a straightforward interpretation of the results in the case of insulating substrates. Only electromagnetic probe or neutral atom diffraction can analyze most systems in a nondisturbing way. However, neutral atoms are only sensitive to the topmost layer of a substrate while, despite its impressive success in the field of surface science, the grazing x-ray-diffraction technique[1] is limited in its application because it implies the use of high intensity synchrotron-radiation sources. Universally used in the field of thin-film growth, near field microscopies as atomic force and scanning tunneling microscopies may imply a perturbation of the growth and are hampered by the tip artefact. Moreover, the rather long time needed to record an image with these methods often prevents them from being used as real time techniques. These limitations likely explain the development of analytical methods based on optical probes for monitoring the growth of a film and determining the thickness of the deposited layers. Indeed, UV visible tools fulfill the *in situ* and nondisturbing conditions for the examination of deposits during their formation, combined with a simple and versatile use on most substrates. In particular, optical methods, which have also the capability of being run in any environment, are widely spread in semiconductor technology.[2]

At the thermodynamical equilibrium, a film wetting the substrate on which it is deposited is expected to grow layer by layer, following a so-called Frank–Van der Merwe growth mode. On the contrary, when a substrate is poorly wetted by the deposited material, three-dimensional clusters are formed in a Volmer-Weber growth mode. In an intermediate case, the Stransky-Krastanov growth mode, the substrate is covered by a few wetting monolayers before the adlayer relaxes to give rise to clusters formation. In addition, in many cases, the morphology of deposited films not only depends on thermodynamics, via the surface and interface energies, but also on kinetics through energy barriers, diffusion coefficients, and intensities of the impinging fluxes. At temperatures and fluxes such that the supersaturation is very high, growth of thin films can give rise to the formation of clusters whose shapes are very far from those expected in equilibrium conditions. Therefore, it is often very hard to distinguish between the different growth modes at the earliest stages of the formation of a film. The knowledge of the cluster mean diameter, aspect ratio, and density during deposition would contribute a breakthrough in the understanding of the growth. In this context, surface differential reflectivity has been proved to be a powerful tool for the determination of the shape ratio[3–5] and of the size of the metallic clusters,[6,7] even within the monolayer range. However, a quantitative analysis of the optical spectra is still at its beginning.[7]

Since the pioneering work of Maxwell Garnett[8] at the turn of the century, there has been large scientific interest in the optical properties of metallic clusters.[9] Their optical behav-

iors are driven to a large extent by the Mie excitations,[10] which can be viewed as surface-plasmon polaritons. If, for isolated clusters with simple shapes, such as spheres or spheroids in vacuum, the exact solution of the Maxwell equation is known, the difficulty of a reliable description of the optical properties of particles dramatically increases for interacting particles of complex shapes, either in a matrix or on a surface. Even though the Maxwell Garnett effective-medium theory and other such theories[11] have been quite successful in tackling these questions, an accurate description of the macroscopic optical properties of the particles, as absorption and reflection, requires a more sophisticated approach than the mean-field theory to find the renormalized polarizability that governs the far-field behavior. Moreover, for clusters deposited on a surface, a quantitative description of the optical properties of the thin film is not only hampered by the interactions between aggregates but also by the mutual interactions between the latter and the substrate.[12,13]

The cluster-substrate and cluster-cluster interactions can be modeled at the dipolar order as in the theory that has been developed by Yamaguchi, Yoshida, and Kinbara.[14,15] The limitations of such an approach, which does not allow for a quantitative description of the size and shape ratio of the clusters of a deposit,[5] prompted Bedeaux and Vlieger[16] to propose a theory, hereafter referred to as the Bedeaux-Vlieger model, to account for the optical behavior of a granular thin film separating two bulk media. This was done by introducing some auxiliary fields named excess fields that enabled one to describe the macroscopic optical effect of the film, with no need of a detailed description of the spatial variations of these quantities as one moves away from boundary layer.[16] The optical properties of the film is essentially related to four surface susceptibilities,[16] which are nothing more than the total integrated excess field. These surface susceptibilities, which are linked to the island polarizabilities for a discontinuous film, govern the Fresnel optical coefficients.[17–20] The modeling of the dipoles arising in clusters under the light excitation relies on the assumption that the mean size of clusters is small compared to the wavelength of the light. Under these conditions, retardation effects, which are related to the finiteness of the speed of light, can be neglected around and inside the islands. Hence, in the electrostatic limit, the Maxwell equations for nonmagnetic materials and the Laplace equation for the electric potential describe the same physics and are thus equivalent. Similar ideas had been put forward earlier by Kretschmann,[21] but using a somewhat different formalism.

This method has been applied to truncated spheres on a substrate by Wind and co-workers.[22,23] The Laplace equation is solved by means of a multipole expansion technique,[24] which consists of placing multipoles at the center of the sphere. The interaction with the substrate is taken into account by introducing image multipoles located at the image point of the multipoles with respect to the surface. The polarizability of the individual islands is then renormalized by taking into account the interactions with the neighboring islands in a self-consistent approximation.[19] This relatively simple model works quite nicely under many circumstances[7,20,25] and may reproduce the main experimental optical features to a large extent (see Sec. II below).

However, while trying to fit optical data corresponding to disk-shaped clusters with an aspect ratio higher than 2, which implies a representation of the clusters by truncated spheres with centers below the surface of the substrate,[5] the numerical computation turns out to be unstable. Beyond the necessity of a general model that could be applied to any case, there appears a need for clear criteria to establish the consistency of the calculation. In the next section, the example of the optical response of a thin silver film deposited on a magnesium oxide substrate allows us to describe in more detail the position of the problem.

II. DIFFERENTIAL REFLECTIVITY ON Ag/MgO(100) FILMS

In a previous paper, it has been reported that UV visible differential reflectance data recorded during the deposit of a silver film on a MgO(100) substrate in vacuum lead to estimates of the size, aspect ratio, and density of the cluster film, which were in excellent agreement with the values derived from an *ex situ* scanning electron microscopy study of the same sample.[7]

A. Experimental setup and results

A silver film of average thickness 2 nm was deposited on a single-crystal MgO(100) held at $T=300\,^{\circ}\mathrm{C}$ under ultrahigh vacuum conditions by Knudsen evaporation. During evaporation, *p*-polarized light (i.e., with the electric field in the plane of incidence) in the UV visible energy range 1–5 eV is impinged at an incident angle of $\theta_0=45°$. The reflected light is recorded in the specular direction. The specular reflectivity $R(\omega)$ can be obtained as function of the frequency ω of the incident light. The recorded relevant quantity is the differential reflection coefficient, which is defined as

$$\frac{\Delta R(\omega)}{R(\omega)}=\frac{R(\omega)-R_F(\omega)}{R_F(\omega)}, \tag{2.1}$$

where $R_F(\omega)$ is the Fresnel reflectivity of the bare substrate. More detailed descriptions of the experimental setup and technique used have already been published.[4,7]

An *ex situ* image of the silver film has been collected by means of a field electron gun–scanning electron microscope (FEG-SEM) shown in Fig. 1(a). As can be seen from this image, the deposit consists of small islands of a linear size of around 10 nm distributed over the surface of the substrate. Such a Volmer-Weber growth mode is expected for the Ag/MgO system since noble metals poorly wet wideband-gap oxide surfaces.[26]

The experimental differential reflectivity spectra at the end of growth is plotted in Fig. 1(b) as function of the photon energy $E=\hbar\omega$ for an incident angle of 45°. The two pronounced resonances seen in this graph are excited by the two components of the *p*-polarized electric field. The low- and high-energy peaks are related to longitudinal and transversal plasma oscillations inside the clusters, respectively.[9] Their positions in energy are mainly governed by the aspect ratio of the islands, which is given by the ratio of height over lateral size, the electromagnetic coupling of the film with the substrate, and the interactions between particles.[4–6]

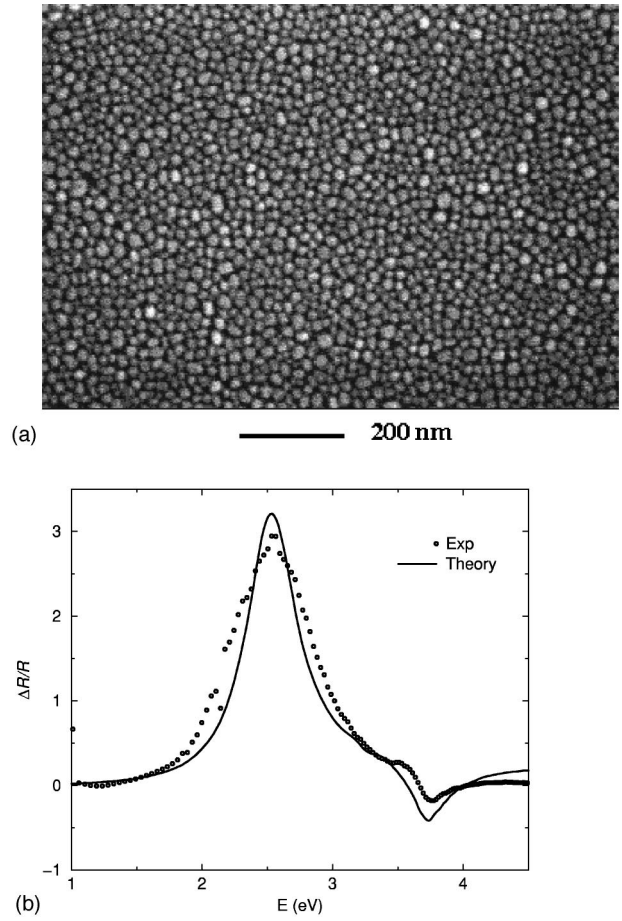

FIG. 1. Experimental data for a 2-nm-thick silver deposit on a magnesium oxide MgO(100) substrate: (a) A FEG-SEM image of the film. The horizontal bar indicated in the figure corresponds to 200 nm; (b) the experimental differential reflectivity spectrum obtained at an incident angle of 45° (circular symbols). A simulation result, using the method of Refs. 22 and 23, is indicated by a solid line and demonstrates good agreement with the experimental data. In the simulation, the truncated spherical particles, of radius $R=6.8$ nm, were placed on a regular grid of lattice constant 19.6 nm, and the truncation parameter (see text) was $t_r=0.11$ (corresponding to an aspect ratio of 1.80). Note that the main spectral features and the numerical values of both the low- and high-energy resonances are well predicted by the theoretical model.

B. Limits of the simulation

The solid curve in Fig. 1(b) represents a simulation result obtained by means of the model[7] derived from the method of Wind and co-workers.[22,23] Within the framework of this theory, deposited islands are modeled by a set of identical truncated spheres that are placed on a regular square array to simplify the calculation since it has earlier been shown that, for low cluster coverages, the optical response of a regular array of clusters with, for example, a square or triangular lattice marginally differs from that of randomly distributed aggregates.[27] Moreover, for such a low cluster density, higher-order interactions between islands are expected to be negligible.[27] The values for the dielectric functions are taken from the literature[28] with, in the case of silver, a correction to account for the finite size of the clusters,[23,9] which reduces the electron mean free path. The island polarizability is evaluated in the quasistatic approximation, the use of which

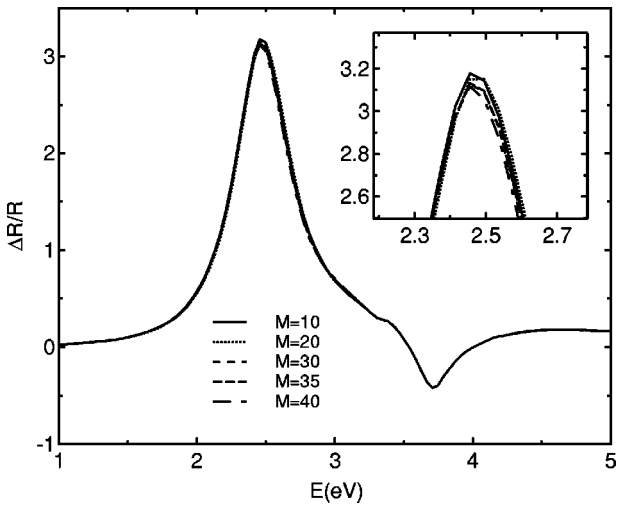

FIG. 2. Simulated differential reflectivity curves $\Delta R(\omega)/R(\omega)$ as a function of energy $E=\hbar\omega$ for different numbers of multipoles included in the simulation. Clusters are defined by the same numerical parameters as in Fig. 1.

is justified by the experimental energy range (1–5 eV, i.e., wavelength in the range 200–1200 nm), by a multipolar development of the potential that is truncated at an order M for numerical reasons. This polarizability is then renormalized by the interisland coupling, which is accounted for only at dipolar order. The model spectrum is chosen by means of a trial and error method, the main emphasis being put on trying to reproduce the location of the low- and high-energy resonances and their intensity.

The theoretical result shown in Fig. 1(b) corresponds to islands represented by spheres of radius $R=6.8$ nm with the center of the sphere located at $0.11R$ above the substrate. The islands are placed on a square lattice with an interisland distance (lattice constant) of 19.6 nm that corresponds to a cluster density of 2.6×10^{11} cm^{-2}. These values nicely compare to those obtained by scanning electron microscopy [Fig. 1(a)], a cluster radius of 8.2 ± 1.5 nm, and a cluster density of $1.9\pm0.5\times10^{11}$ cm^{-2}[9]. The silver coverage that can be derived from the optics compares within a few percent with that obtained from the SEM image. Such quantitative agreement is impressive, in particular, in view of the relative simplicity of the model on which the simulation is based.

The best fit between the optical spectrum and the model has been found[7] for an aspect ratio (diameter to height) of 1.8 [Fig. 1(b)]. Numerical results are shown in Fig. 2 as a function of the multipole order within this particular geometry. A good convergence is obtained upon increasing the multipole order. The same is observed for any case in which the aspect ratio of the deposited cluster is lower than 2 (i.e., when the center of the sphere is above the surface of the substrate). However, when performing the calculation for truncated spheres with centers below the surface of the substrate, the numerical code does not converge any longer. An example is given in Fig. 3 where the model is applied to a cluster geometry similar to that used in Fig. 2 except for the aspect ratio, which is now set at a value of 2.2. Upon including higher and higher multipole orders in the simulations, the position of the low-energy resonance is wandering and shows no trend of convergence. At this stage, two cases

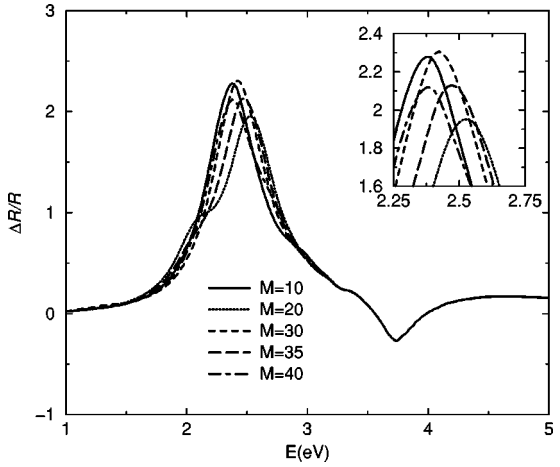

FIG. 3. Simulated differential reflectivity by the Bedeaux-Vlieger truncated spherical model for the same island parameters as in Fig. 1 but for a negative truncation ratio $t_r=-0.11$ (aspect ratio of 2.25). The various curves correspond to different choices for the multipole order as indicated in the legend of the figure. Note that in the region around the low-energy resonance no convergence seems to be reached by increasing the number of multipoles included in the calculation. The inset shows the details of the differential reflectivity curves around the low-energy resonance.

ought to be considered. When the center of the sphere is beyond the mid distance between the surface of the substrate and the bottom of the sphere, the divergence of the calculation happens for mathematical reasons since the image point is outside the physical domain or, in other words, outside the sphere. In a different way, when the image point is within the sphere, solutions might exist. The lack of convergence likely arises from the conditioning of the matrix. Indeed, the problem cannot be solved by increasing the number of multipoles since, at some stage, the machine accuracy is overflowed. In both cases, a suggestion to find out favorable configurations in which the numerical calculation could be performed more successfully is to move the expansion center. This point will be examined in Sec. III.

Nevertheless, neither the convergence of the model itself nor that of the model with the experimental data can guarantee the correctness of the solution. These are only indirect proofs. In the model, potentials are expressed as a function of expansion coefficients up to the Mth order, although the optical response, which is derived from the dipole polarizability of the deposited clusters, only relies on the first-order expansion coefficients. Therefore, the convergence of the calculated optical response is necessary but not sufficient to validate the expressions of the potentials. At variance, the boundary conditions depend on all the expansion coefficients until the highest order, so that a definite evidence of the consistency of the model would be gained by their fulfillment. The question will be addressed in Sec. IV where the above Ag/MgO case will be used to test the accuracy of the model.

III. A MODEL FOR EVALUATING ISLAND POLARIZABILITIES

The cluster geometry used in the present paper, which is derived from that used by Bedeaux and co-worker is depicted in Fig. 4. It consists of a substrate (medium 2) localized in vacuum (medium 1) and covered with clusters (medium 3) whose size is assumed to be small with respect to the wavelength of the incident light. The islands are modeled by truncated spheres of radius R. The vacuum-substrate interface is located at $z=D$, with $-R<D<R$. The plane that passes through the center of the sphere is defined by $z=0$. The dimensionless truncation parameter t_r,

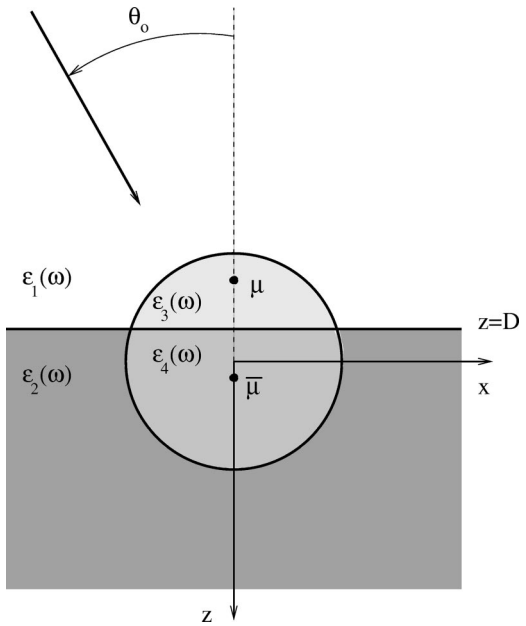

FIG. 4. The cross section of the geometry considered in the present work. Here μR indicates the z coordinate of the location of the multipoles, while $\bar{\mu}R$ is the same quantity but for the image multipoles. Note that the multipoles and thus also the image multipoles are always located on the z axis, which is the axis of revolution. The position of the substrate is parallel to the xy plane, and it is located at $z=D$, where D is a (signed) real constant. The dielectric functions of the various regions are those indicated in the figure by $\varepsilon_i(\omega)$, with $i=1,\ldots,4$.

$$t_r=\frac{D}{R}\ (-1<t_r<1), \tag{3.1}$$

describes the degree of truncation. For technical reasons which would become apparent below, the part of the spheres lying below the interface is introduced as a distinct medium (medium 4). This latter medium will finally be attributed properties identical to the substrate (medium 2). A main spherical coordinate system, $\mathcal{S}$, is defined such that the origin of the radial coordinate r coincides with the center of the sphere (Fig. 4). The polar and azimuthal angles are θ and ϕ, respectively. The positive z axis, which is also the axis of revolution of the system, is pointing downwards into the substrate. The impinging light of wavelength λ scatters at the surface at an incidence angle θ_0. To calculate the island polarizability, the polarization of the islands by the incident light is modeled by using a multipolar expansion and by introducing the image multipoles with respect to the substrate.[22] The center of the potential expansion is chosen along the z axis at a position μR in the main coordinate system $\mathcal{S}$, with

$$-1<\mu<1. \tag{3.2}$$

The image multipole position becomes $\bar{\mu}R$, where

$$\bar{\mu}=2t_r-\mu. \tag{3.3}$$

It is convenient to introduce two other coordinate systems, $\mathcal{S}_\mu$ and $\mathcal{S}_{\bar{\mu}}$, whose origins are located at the multipole and multipole image centers, respectively. The azimuthal angle of the plane of incidence of the light is defined as ϕ_0. It is taken equal to zero in all the numerical calculations, which are performed herein.

A. Multipole expansions of the potential

If the linear dimension of the island is small compared to the wavelength of the incident light, retardation effects in and around the island can safely be neglected. If the island material is assumed to be nonmagnetic, then the incident magnetic field will be unaffected. Hence the main field is the electric field $\mathbf{E}(\mathbf{r})$, which is related to the potential $\psi(\mathbf{r})$ in the usual way $\mathbf{E}(\mathbf{r})=-\boldsymbol{\nabla}\psi(\mathbf{r})$. When retardation effects can be neglected or, in other words, when the size of the island is supposed to be much smaller than the wavelength, this potential must only satisfy the Laplace equation

$$\boldsymbol{\nabla}^2\psi(\mathbf{r})=0. \tag{3.4}$$

The appropriate boundary conditions for this potential come from the continuity of the potential itself and of the normal components of the displacement field,

$$\psi_I(\mathbf{r}_s)=\psi_{II}(\mathbf{r}_s), \tag{3.5a}$$

$$\varepsilon_I(\omega)\partial_n\psi_I(\mathbf{r}_s)=\varepsilon_{II}(\omega)\partial_n\psi_{II}(\mathbf{r}_s). \tag{3.5b}$$

Here $\varepsilon_i(\omega)$ is the frequency dependent dielectric function of medium i, $\mathbf{r}_s$ is assumed to be any point on the interface, and ∂_n denotes its normal derivative. These conditions should be fulfilled for any two media having a common interface.

To solve Eq. (3.4), with the boundary conditions [Eqs. (3.5)], it is convenient to use[25] a multipole expansion for the potentials. In medium 1, the potential then takes the form

$$\psi_1(\mathbf{r})=\psi_0(\mathbf{r})+\sum_{l,m}^{l\neq 0}A_{lm}r_\mu^{-l-1}Y_{lm}(\theta_\mu,\phi_\mu)+\sum_{l,m}^{l\neq 0}A^R_{lm}r_{\bar{\mu}}^{-l-1}Y_{lm}(\theta_{\bar{\mu}},\phi_{\bar{\mu}}). \tag{3.6}$$

The spherical coordinates $(r_\mu,\theta_\mu,\phi_\mu)$ and $(r_{\bar{\mu}},\theta_{\bar{\mu}},\phi_{\bar{\mu}})$ are referring to the coordinate systems $\mathcal{S}_\mu$ and $\mathcal{S}_{\bar{\mu}}$, which are centered at the points μ and $\bar{\mu}$, respectively (Fig. 4). The m summation will be understood to range from $m=-l$ to l. The spherical harmonics $Y_{lm}(\theta,\phi)$ are normalized according to the convention[29]

$$Y_{lm}(\theta,\phi)=\sqrt{\frac{2l+1}{4\pi}\frac{(l-m)!}{(l+m)!}}P_l^m(\cos\theta)(-1)^m e^{im\phi}, \tag{3.7}$$

where $P_l^m(\cos\theta)$ are the associated Legendre polynomials defined as[29]

$$P_l^m(x)=\frac{(1-x^2)^{m/2}}{2^l l!}\frac{d^{l+m}}{dx^{l+m}}(x^2-1)^l,\quad x=\cos\theta, \tag{3.8}$$

for $m\geq 0$, while for $m<0$,

$$P_l^m(x)=(-1)^m\frac{(l+m)!}{(l-m)!}P_l^{-m}(x). \tag{3.9}$$

In Eq. (3.6), $\psi_0(\mathbf{r})$ stands for the potential corresponding to the incident field $\mathbf{E}_0$, which, provided clusters are small compared to the wavelength of the light, can be approximated by a homogeneous field

$$\mathbf{E}_0=E_0(\sin\theta_0\cos\phi_0,\sin\theta_0\sin\phi_0,\cos\theta_0). \tag{3.10}$$

The potential $\psi_0(\mathbf{r})$ related to this incident field then takes the following form:

$$\begin{aligned}\psi_0(\mathbf{r})&=-rE_0(\cos\theta\cos\theta_0+\sin\theta\cos\phi\sin\theta_0\cos\phi_0\\&\quad+\sin\theta\sin\phi\sin\theta_0\sin\phi_0)\\&=-rE_0\sqrt{\frac{2\pi}{3}}\{\sqrt{2}\cos\theta_0Y_{10}(\theta,\phi)\\&\quad-\sin\theta_0[e^{-i\phi_0}Y_{11}(\theta,\phi)-e^{i\phi_0}Y_{1-1}(\theta,\phi)]\},\end{aligned} \tag{3.11}$$

with $E_0=|\mathbf{E}_0|$. The spherical coordinates (r,θ,ϕ) are defined with respect to the coordinate system $\mathcal{S}$ whose origin is at the center of the sphere.

For the potential inside the substrate, the solution of the Laplace equation is chosen as

$$\begin{aligned}\psi_2(\mathbf{r})&=a_0-rE_0\sqrt{\frac{2\pi}{3}}\{\sqrt{2}a_1\cos\theta_0Y_{10}(\theta,\phi)\\&\quad-\sin\theta_0[a_2e^{-i\phi_0}Y_{11}(\theta,\phi)-a_3e^{i\phi_0}Y_{1-1}(\theta,\phi)]\}\\&\quad+\sum_{l,m}^{l\neq 0}A^T_{lm}r_\mu^{-l-1}Y_{lm}(\theta_\mu,\phi_\mu),\end{aligned} \tag{3.12}$$

where a_i are constants to be determined. Note that the terms inside the curly brackets are a linear combination of the terms involved in the expression (3.10) of the potential $\psi_0(\mathbf{r})$. For the potential inside the cluster, medium 3 and 4, the following expansions are defined as

$$\psi_3(\mathbf{r})=b_0+\sum_{l,m}^{l\neq 0}B_{lm}r_\mu^lY_{lm}(\theta_\mu,\phi_\mu)+\sum_{l,m}^{l\neq 0}B^R_{l,m}r_{\bar{\mu}}^lY_{lm}(\theta_{\bar{\mu}},\phi_{\bar{\mu}}), \tag{3.13a}$$

$$\psi_4(\mathbf{r})=b_0'+\sum_{l,m}^{l\neq 0}B^T_{lm}r_\mu^lY_{lm}(\theta_\mu,\phi_\mu), \tag{3.13b}$$

where b_0 and b_0' are constants to be determined.

B. Determination of the expansion coefficients via boundary conditions

The various unknown expansion coefficients, a_i, A_{lm}, B_{lm}, etc., are now calculated in terms of the known parameters of the model by imposing the boundary conditions on the considered geometry. Since a formulation with image multipoles is used, the boundary conditions at $z=D$ are easily satisfied. Their fulfillment leads to the following relations:

$$a_0 = E_0 d\left(\frac{\varepsilon_1}{\varepsilon_2} - 1\right)\cos\theta_0, \tag{3.14a}$$

$$a_1 = \frac{\varepsilon_1}{\varepsilon_2}, \tag{3.14b}$$

$$a_2 = a_3 = 1, \tag{3.14c}$$

$$A_{lm}^R = (-1)^{l+m}\frac{\varepsilon_1 - \varepsilon_2}{\varepsilon_1 + \varepsilon_2} A_{lm}, \tag{3.14d}$$

$$A_{lm}^T = \frac{2\varepsilon_1}{\varepsilon_1 + \varepsilon_2} A_{lm}. \tag{3.14e}$$

The continuity at the same boundary $(z=D)$, but now inside the sphere, gives

$$b_0 = b_0', \tag{3.15a}$$

$$B_{lm}^R = (-1)^{l+m}\frac{\varepsilon_3 - \varepsilon_4}{\varepsilon_3 + \varepsilon_4} B_{lm}, \tag{3.15b}$$

$$B_{lm}^T = \frac{2\varepsilon_3}{\varepsilon_3 + \varepsilon_4} B_{lm}. \tag{3.15c}$$

An explicit expression for the constant b_0 is given in Eq. (A12) of the Appendix. These results are obtained by taking advantage of both the orthogonality of the spherical harmonics and the fact that on the surface of the substrate $(z=D)$, as a consequence of the symmetry of the location of the multipoles and image multipoles, the following relations hold: $r_\mu = r_{\bar{\mu}}$, $\theta_\mu = \pi - \theta_{\bar{\mu}}$, and $\phi_\mu = \phi_{\bar{\mu}}$. Note that the relations (3.14), (3.15) are independent of the location of the multipoles, so that they are similar to those obtained by Wind, Vlieger, and Bedeux[22] under the assumption that the multipoles are located at the center of the sphere. Finally, there are only two independent classes of expansion coefficients, namely A_{lm} and B_{lm}.

These coefficients can be derived from the relations that express the fulfillment of the boundary conditions at the surface of the sphere, where $r=R$. By multiplying all the terms of those relations by the complex-conjugate spherical harmonic $[Y_{lm}(\theta,\phi)]^*$ and by integrating the resulting expressions over the surface of the sphere, where one again takes advantage the orthogonality of the spherical harmonics, the following (infinite) set of equations is obtained:

$$\sum_{l'=1}^{\infty} [C_{ll'}^m R^{-l'-2} A_{l'm} + D_{ll'}^m R^{l'-1} B_{l'm}] = H_l^m, \tag{3.16a}$$

$$\sum_{l'=1}^{\infty} [F_{ll'}^m R^{-l'-2} A_{l'm} + G_{ll'}^m R^{l'-1} B_{l'm}] = J_l^m, \tag{3.16b}$$

where $l=1,2,\ldots,$ and $m=0,1$. The various matrix elements of the above linear system can all be found in the Appendix, where their detailed derivation also is presented. The above linear system has only a nontrivial solution when $m=0$ and $m=\pm 1$ [cf. Eqs. (A4)]. These values are associated with the components of the uniform incident field $\mathbf{E}_0$, which are orthogonal and parallel to the substrate, respectively. An additional simplification can be made by showing that the equations corresponding to $m=-1$ and $m=1$, respectively, are equivalent.

To allow for a numerical solution of the infinite linear system (3.16), an upper cutoff M in l and l' has to be introduced. The integrals that define the system of equations (A5) are computed by Gauss-Legendre numerical integration. Solutions of the linear system lead to values of the expansion coefficients A_{lm} and B_{lm}, which in turn can be directly related to the (dipole) polarizability of the island. These can be shown to be given by[23]

$$\alpha_\perp = \frac{2\pi\varepsilon_1 A_{10}}{\sqrt{\frac{\pi}{3}} E_0 \cos\theta_0}, \tag{3.17a}$$

$$\alpha_\parallel = -\frac{4\pi\varepsilon_1 A_{11}}{\sqrt{\frac{2\pi}{3}} E_0 \sin\theta_0 \exp(-i\phi_0)}. \tag{3.17b}$$

Here $\alpha_\perp$ and $\alpha_\parallel$ are the dipole polarizabilities perpendicular and parallel to the interface of the substrate, respectively. Due to the presence of the substrate, these are in general quite different. In the present work, the parameter of interest is the differential optical reflectivity $\Delta R(\omega)/R(\omega)$ defined in Sec. II. This quantity is evaluated by modified Fresnel formulas for reflection where the above given polarizabilities appear through the surface susceptibilities.[16]

The present section was aimed at introducing a general method for the calculation of the polarizability of truncated spheres supported by a substrate. The model of Wind and co-workers[22,23] is just a special case of this approach with $\mu=0$ (see the Appendix for details), at least for $t_r \geq 0$. Indeed, to obtain the solution for the case in which the center of the sphere is located below the substrate $(t_r<0)$, these authors[22,23] apply to the $(t_r>0)$ case a coordinate transformation method with a permutation of the dielectric constants. This implies that different potential expansions are used in the two cases, while, in the present work, the expansions in use do not depend on the location of the multipoles with respect to the surface. Criteria are now needed to know how reliable these models are, with special attention being paid to cases corresponding to negative values of the truncation ratio t_r.

IV. FULFILLMENT OF THE BOUNDARY CONDITIONS

In Sec. II and in the already published work,[7] the method has only been judged on the basis of the convergence of the differential reflectivity curves $\Delta R(\omega)/R(\omega)$. Indeed, in the model used herein, the reflectivity only relies on the lowest-order expansion coefficient A_{10} and A_{11} [cf. Eqs. (3.17)]. Therefore, the occurrence of a convergence of the reflectivity curves upon, say, increasing the multipole order M, does not provide any proof of the reliability of the potentials since these depend on all the expansion coefficients up to the cut-off order. The potentials given by the expansions (3.6), (3.12), and (3.13), can in principle be calculated in any point of space provided the multipole coefficients, A_{lm} and B_{lm}, are known. Since the multipole expansions are indeed solutions of Eqs. (3.4) and (3.5) at any M, it is only the fulfillment of the boundary conditions at the interface between the various media that has to be checked. It has to be stressed that this fulfillment is a more severe test for the calculation than just considering the convergence of the differential reflectivity curves. It is not only the self-consistency of the numerical implementation but that of the method itself that is controlled. Such a study thus provides a powerful and rigorous tool for justifying the quality of previous and present numerical simulations based on a multipole expansion.

The calculation including the multipoles and their images, the boundary conditions at the cluster-substrate interface, are obeyed by construction. Thus, the only boundary conditions to be checked are at the surface of the sphere. To measure the error in these, two error functions are defined,

$$\mathcal{E}_{\psi}(\mathbf{r}_s)=\frac{\psi_+(\mathbf{r}_s)-\psi_-(\mathbf{r}_s)}{\max_{\mathbf{r}_s}\psi_0(\mathbf{r}_s)}, \tag{4.1a}$$

$$\mathcal{E}_{\partial_n\psi}(\mathbf{r}_s)=\frac{\varepsilon_+\partial_n\psi_+(\mathbf{r}_s)-\varepsilon_-\partial_n\psi_-(\mathbf{r}_s)}{\max_{\mathbf{r}_s}[\varepsilon\,\partial_n\psi_0(\mathbf{r}_s)]}. \tag{4.1b}$$

The subscripts $+$ $(-)$ correspond to quantity just outside (inside) the surface of the sphere. The maximum value of the incidence potential ψ_0 at the surface of the sphere, and the corresponding quantity for the normal derivative, are used as normalization factors. The impact of the parameters of the model, location of the multipole center, photon energy, and multipole order on the accuracy of the numerical calculations is examined in the following by considering the values taken by the error functions in various representations of the above-mentioned Ag/MgO deposit.

A. Location of the expansion center

In the model put forward in the present paper, the multipole expansion point can move along the symmetry z axis, instead of being at the center of the sphere as in the Bedeaux-Vlieger model. In Fig. 5, an attempt is made to determine the optimal position μ for a given truncation ratio and value of $M=20$ at an energy of $E=4.5$ eV. The mean spatial absolute error in the boundary conditions $\langle|\mathcal{E}_{\psi}(\mathbf{r}_s)|\rangle$ and $\langle|\mathcal{E}_{\partial_n\psi}(\mathbf{r}_s)|\rangle$, which are defined in Eq. (4.1), are shown in Fig. 5 as function of the truncation ratio. It can be observed that the value of μ, which leads to the minimum error, depends on the truncation ratio. For $t_r\geqslant 0$, the Bedeaux-Vlieger limit, where $\mu=0$, provides the minimum error whereas, for $t_r\leqslant 0$, an improvement is obtained by moving the expansion point inside the physical domain or, in other words, by using negative μ values. However, for negative truncation ratios, the matrix system becomes dramatically more and more ill conditioned; a fact that may be due to intervention of an increasing power of distance between the surface of the sphere and the expansion points μ and $\bar{\mu}$.

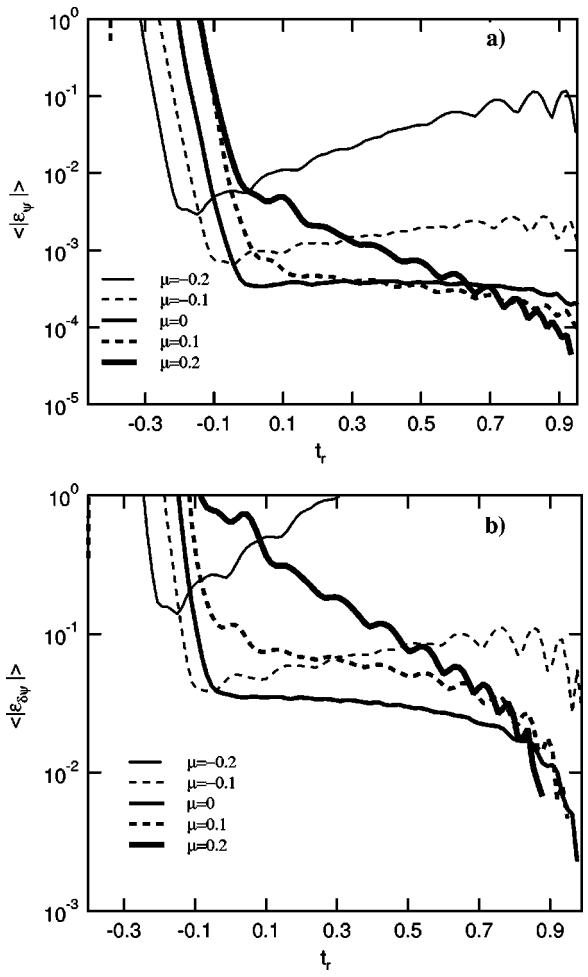

FIG. 5. The mean errors as defined in the text, $\langle|\mathcal{E}_{\psi}(\mathbf{r}_s)|\rangle$ and $\langle|\mathcal{E}_{\partial_n\psi}(\mathbf{r}_s)|\rangle$, in the boundary conditions of (a) the potential and (b) its normal derivative, as function of t_r for different μ values. The model clusters are defined with the same parameters as in the Ag/MgO(100) case (Fig. 1), with $E=4.5$ eV and $M=20$.

In principle, the infinite expansion of potentials on which the method is based should lead to a unique numerical value, wherever the location of the expansion center is. In the case of numerical calculations, where the expansion is truncated at an order M, it is not too surprising to find, for a given value of M, a (weak) dependency of the error functions on the position of the expansion point, as already stressed in Fig. 5. A search for an optimal position of the expansion center can be performed for each value of the truncation ratio (Fig. 6). For $t_r\geqslant 0$ (see also Fig. 5), it is the center of the sphere ($\mu=0$). For $t_r\leqslant 0$, it appears that the best choice is to place the μ point close to the substrate so that $\mu=t_r$, that is to say to superimpose the center of expansion and its image. Roughly speaking, for $t_r\leqslant 0$, between one and two or-

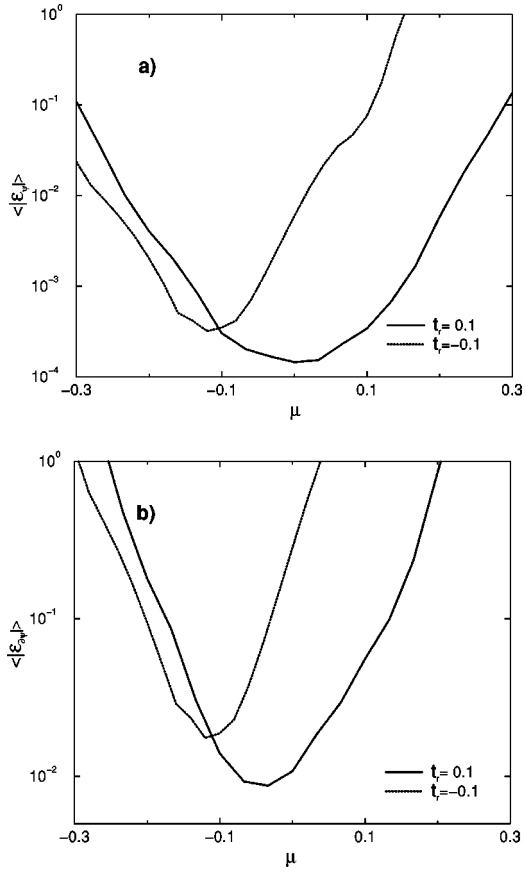

FIG. 6. Fulfillment of the boundary conditions as function of μ for an energy $E=4.5$ eV, a multipole order $M=20$, and two given values of t_r, 0.1, and -0.1. Error functions on (a) the potential and (b) the normal derivative.

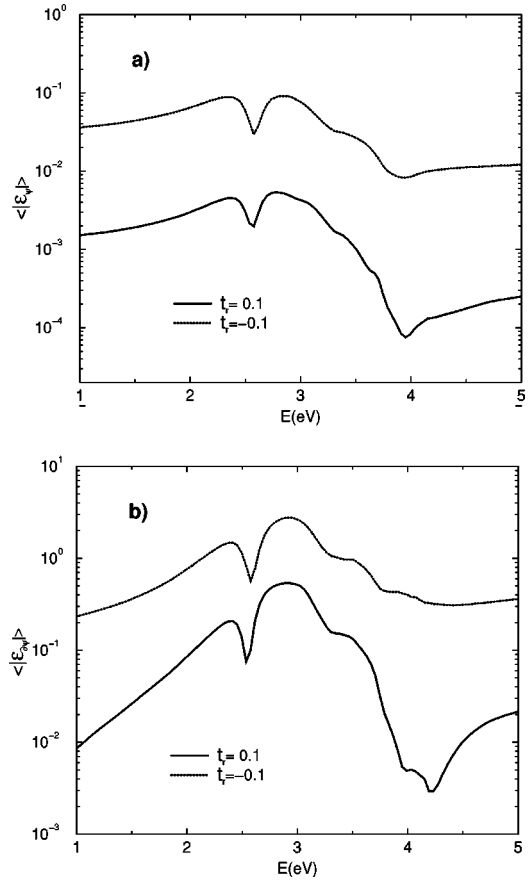

FIG. 7. The mean error in the boundary conditions as a function of energy for two values of $t_r=0.1$ and $t_r=-0.1$, in the case defined by $\mu=0$ and $M=20$, for (a) the potential and (b) the normal derivative.

ders of magnitude in the error function can be earned by the present method with respect to the Bedeaux-Vlieger model in which $\mu=0$.

B. Boundary conditions at the resonance energy

When the energy of the incident light is close to a resonance of the system, i.e., in our case, close to either the low-energy resonance around 2.5 eV or the high-energy resonance at 3.7 eV, the boundary conditions are even harder to satisfy. This is seen from Fig. 7 where the (spatial) mean of the absolute error in the boundary conditions, $\langle|\mathcal{E}_\psi(\mathbf{r}_s)|\rangle$ and $\langle|\mathcal{E}_{\partial_n\psi}(\mathbf{r}_s)|\rangle$, are shown as function of energy $E=\hbar\omega$ for truncation ratio $t_r=0.1$ and $t_r=-0.1$. The dips that can be observed around the low-energy resonance at $E=2.5$ eV are believed to come from numerical artefacts. These figures highlight the sizable effect of the dielectric function on the quality of the simulation, since the energy range $E=2$ eV to $E=3.7$ eV, where the resonances are peaking, concentrates on the highest values of the error functions. This is, however, probably not so surprising in view of the fact that the system is close to singular at a resonance point. As the truncation ratio is reduced, the overall error seems to be increased, but it is still the regions around the resonances that are associated with the largest errors. Roughly speaking, the errors in the boundary conditions are raised by an energy independent factor as the truncation ratio is reduced (Fig. 7).

C. Multipole order

By increasing the number of multipoles included in the calculation M the fulfillment of the boundary conditions should be improved since the size of the function basis increases. Figure 8 shows the errors $\langle|\mathcal{E}_\psi(\mathbf{r}_s)|\rangle$ and $\langle|\mathcal{E}_{\partial_n\psi}(\mathbf{r}_s)|\rangle$ as function of M for the energy $E=4.5$ eV and $\mu=0$ for two truncation ratios $t_r=0.1$ and $t_r=-0.1$. These figures are representative of the cases where $\mu=0$. For $t_r\geqslant 0$, the error decreases upon increasing M, which corresponds to the expected behavior. However, for $t_r\leqslant 0$, the error is not seen to decrease upon increasing M. In this case, the error functions are quite sensitive to the value of μ. This is illustrated in Fig. 9 where the error functions are given for μ values of 0 and -0.1. It is observed that moving the expansion point away from the center of the sphere may dramatically improve the overall error made in the simulation. Finally, it can be noted that, in all cases, a higher limit in M is imposed by the vanishing of the matrix conditioning.

D. Spatial variations of the error functions

The evolutions of the potential ψ and of its normal derivative $\varepsilon\partial_n\psi$ along the surface of the sphere, in the plane of incidence of the light [Figs. 10(a) and 10(b)] and in a plane perpendicular to it [Figs. 10(c) and 10(d)], are given as function of the polar angle θ in Fig. 10 for the case corresponding

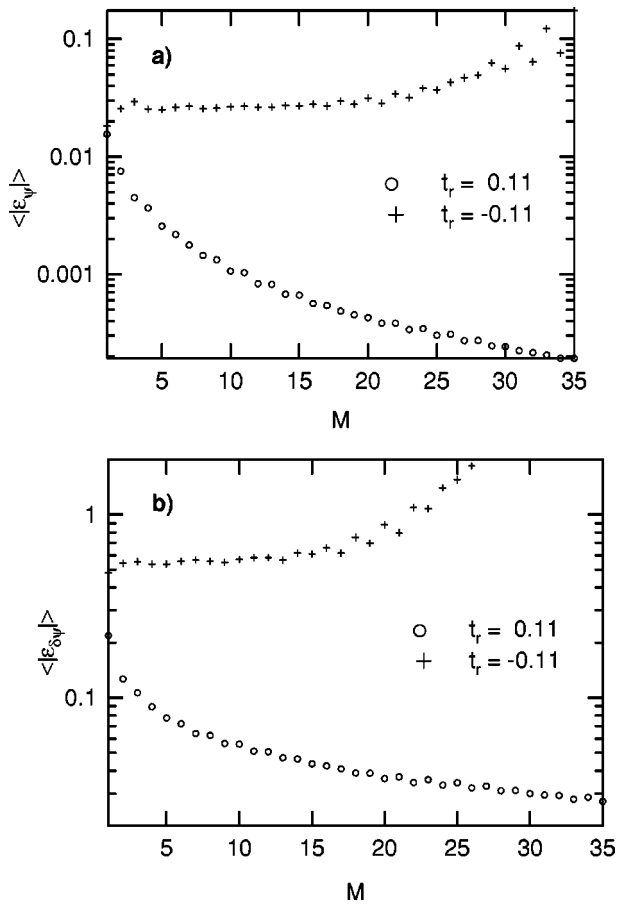

FIG. 8. The evolution of the error in the boundary conditions as a function of the order in the multipole development in the case of which $E=4.5$ eV, $\mu=0$, for two given values of t_r, 0.1, and -0.1 [(a) potential (b) the normal derivative].

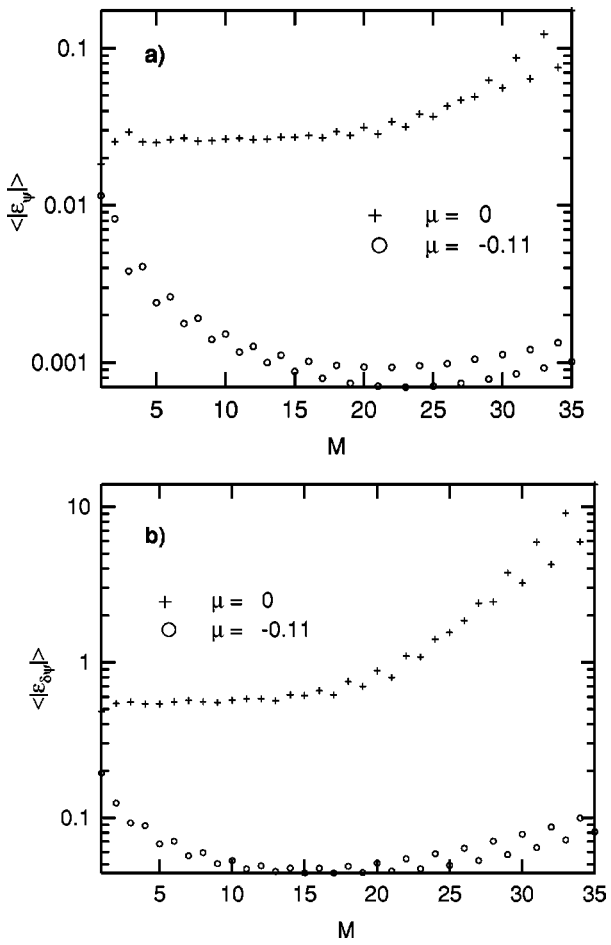

FIG. 9. The improvement brought in the convergence of the boundary conditions by moving the expansion point in the case $t_r=-0.1$, $E=4.5$ eV as a function of the multipole order M.

to $t_r=0.1$, $E=4.5$ eV, $\mu=0$, and $M=16$. Also shown are the error functions $\langle|\mathcal{E}_\psi(\mathbf{r}_s)|\rangle$ [Figs. 10(a) and 10(c)] and $\langle|\mathcal{E}_{\partial_n\psi}(\mathbf{r}_s)|\rangle$ [Figs. 10(b) and 10(d)] in the bottom panels of the graphs. For the same set of parameters, we have also found (results not shown) that the errors are slowly varying functions of the azimuthal angle ϕ. The regions that give rise to the largest errors in the boundary conditions are concentrated around the top of the sphere and, to some extent, at the interface between the spherical cap and the substrate. The same trends can be observed in the global view of the boundary conditions, which is presented in Fig. 11 for the same case. This view consists of a projection in the plane of incidence of $\langle|\mathcal{E}_\psi(\mathbf{r}_s)|\rangle$ (upper panel) and $\langle|\mathcal{E}_{\partial_n\psi}(\mathbf{r}_s)|\rangle$. The direction of the incidence of the light is indicated by an arrow. The error is roughly of the same order of magnitude all over the sphere.

V. CONCLUSIONS

A generalized method for the calculation of the polarizability of a truncated sphere by means of a multipolar description has been presented. The proposed approach, which is an extension of earlier published works due to Bedeaux, Vlieger, and co-workers[22,23] and which contains this model as a special case, is based on the possibility for the multipole expansion center to freely move along the z axis of the main coordinate system instead of being located at the center of the sphere. This method allows us to perform the calculations for cases in which the numerical code is poorly conditioned when the center of the truncated sphere is below the plane of truncation. Let us stress that this geometry has a strong importance since it corresponds to clusters whose aspect ratio is higher than 2.

Neither the convergence of the model itself nor the agreement between the data and the model can guarantee that the solution is correct, since the reflectivity curves only depend on the lowest-order expansion coefficients. A way to assess the quality of the numerical calculation to the upper order has been introduced, which consists of judging the accuracy of the models on the basis of fulfillment of the appropriate boundary conditions. It is shown that, provided the cluster aspect ratio is not too high, the multipole expansion method represents a rather accurate tool for the determination of mean values of the parameters characterizing the deposited clusters. In all cases however, the values found for the error functions allow us to estimate the validity of the model. The simulation of the optical reflectivity in the UV visible range allows us to determine cluster size, shape ratio, and density in a rather accurate manner, as illustrated herein by the case of a Ag/MgO(100) deposit. The method offers a promising tool for the *in situ* examination of cluster growth on substrates.

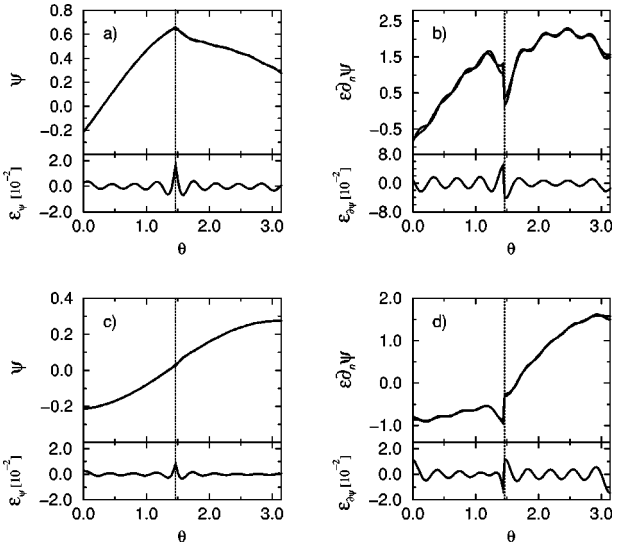

FIG. 10. Evolution of the potential [(a) and (b)] and its normal derivative [(c) and (d)] along the surface of the sphere. The errors in the boundary conditions of the potential on the surface of the sphere, $\mathcal{E}_{\psi}(\mathbf{r}_s)$ [(a) and (c)] and of the normal derivative $\mathcal{E}_{\partial_n\psi}(\mathbf{r}_s)$ [(b) and (d)], are shown as function of the spherical coordinate θ for given value of the azimuthal angle ϕ. The values used for the angle ϕ correspond to the incident plane ($\phi=0$) [(a) and (b)] and a plane perpendicular to the incident plane ($\phi=\pi/2$) [(c) and (d)]. The energy of the incident light is $E=4.5$ eV, the truncation ratio is $t_r=0.1$ (and $\mu=0$), and the number of multipoles is $M=16$.

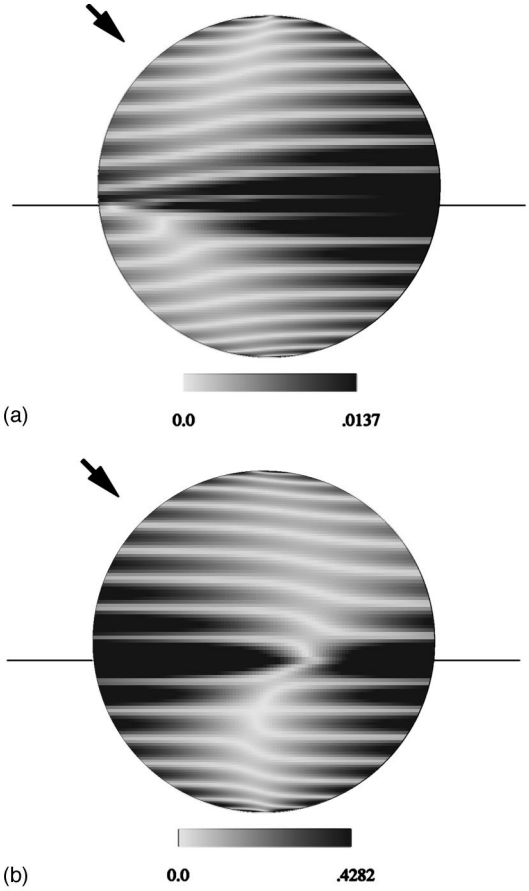

FIG. 11. Global view of the boundary condition errors (a) $\langle|\mathcal{E}_{\psi}(\mathbf{r}_s)|\rangle$ and (b) $\langle|\mathcal{E}_{\partial_n\psi}(\mathbf{r}_s)|\rangle$ when projected into the plane of incidence. The parameters used are $E=4.5$ eV, $t_r=0.1$, and $M=20$.

ACKNOWLEDGMENTS

One of the authors (I.S.) would like to thank D. Bedeaux for invaluable discussions and for kindly making available unpublished notes regarding the topic of thin discontinuous films. I.S. would also like to thank the Research Council of Norway (Contract No. 32690/213), Norsk Hydro ASA, Total Norge ASA, CNRS (Center National de la Recherche Scientifique), and R.L. acknowledges Saint-Gobain Recherche for financial support.

APPENDIX: THE MATRIX ELEMENTS

In this appendix we give the various matrix elements, and the form of the right-hand side, appearing in the matrix system [Eqs. 3.16)]. With the particular expansions chosen for the potentials $\psi_i(\mathbf{r})$ ($i=1,2,3,4$) (cf. Sec. III), and the relations Eqs. (3.14) and (3.15), the boundary conditions at the surface of the substrate, by construction, are automatically fulfilled. However, we still need to satisfy the remaining boundary conditions [Eqs. (3.5)] on the surface of the sphere. By taking these boundary conditions, multiplying by the complex-conjugate spherical harmonic $[Y_{lm}(\theta,\phi)]^*$, and integrating over all directions, i.e., using the weak formulation of the boundary conditions, one is lead to the following matrix system [cf. Eqs. (3.16)]:

$$\sum_{l'=1}^{\infty}\left[C^m_{ll'}R^{-l'-2}A_{l'm}+D^m_{ll'}R^{l'-1}B_{l'm}\right]=H^m_l, \quad \text{(A1a)}$$

$$\sum_{l'=1}^{\infty}\left[F^m_{ll'}R^{-l'-2}A_{l'm}+G^m_{ll'}R^{l'-1}B_{l'm}\right]=J^m_l. \quad \text{(A1b)}$$

This linear system can be used to determine the expansion coefficients A_{lm} and B_{lm} for all allowed values of l and m: $l=0,\pm1,\pm2,\ldots$ and $m=0,\pm1,\pm2,\ldots,\pm m$. However, for orthogonality reasons on integration over ϕ, this system is reduced to $m=-1,0,1$, since only the (uniform) incident field contains these ''quantum numbers'' [cf. Eq. (3.11)]. The matrix elements of the system [Eqs. A1)] are thus given by the expressions

$$C^m_{ll'}=\zeta^m_{ll'}\left[K^m_{ll'}[\mu](t_r)+\frac{\varepsilon_1-\varepsilon_2}{\varepsilon_1+\varepsilon_2}(-1)^{l'+m}K^m_{ll'}[\bar{\mu}](t_r)+\frac{2\varepsilon_1}{\varepsilon_1+\varepsilon_2}\{K^m_{ll'}[\mu](t_r=1)-K^m_{ll'}[\mu](t_r)\}\right], \quad \text{(A2a)}$$

$$D^m_{ll'}=-\zeta^m_{ll'}\left[M^m_{ll'}[\mu](t_r)+\frac{\varepsilon_3-\varepsilon_4}{\varepsilon_3+\varepsilon_4}(-1)^{l'+m}M^m_{ll'}[\bar{\mu}](t_r)+\frac{2\varepsilon_3}{\varepsilon_3+\varepsilon_4}\{M^m_{ll'}[\mu](t_r=1)-M^m_{ll'}[\mu](t_r)\}\right], \quad \text{(A2b)}$$

$$F^m_{ll'}=\zeta^m_{ll'}\left[\frac{2\varepsilon_1\varepsilon_2}{\varepsilon_1+\varepsilon_2}L^m_{ll'}[\mu](t_r=1)+\varepsilon_1\frac{\varepsilon_1-\varepsilon_2}{\varepsilon_1+\varepsilon_2}\{L^m_{ll'}[\mu](t_r)+(-1)^{l'+m}L^m_{ll'}[\bar{\mu}](t_r)\}\right], \quad \text{(A2c)}$$

and

$$G^m_{ll'}=-\zeta^m_{ll'}\left[\frac{2\varepsilon_3\varepsilon_4}{\varepsilon_3+\varepsilon_4}N^m_{ll'}[\mu](t_r=1)+\varepsilon_3\frac{\varepsilon_3-\varepsilon_4}{\varepsilon_3+\varepsilon_4}\{N^m_{ll'}[\mu]\times(t_r)+(-1)^{l'+m}N^m_{ll'}[\bar{\mu}](t_r)\}\right]. \quad \text{(A2d)}$$

Here the following notation has been introduced:

$$\zeta^m_{ll'}=\frac{1}{2}\sqrt{\frac{(2l+1)(2l'+1)(l-m)!(l'-m)!}{(l+m)!(l'+m)!}}, \quad \text{(A3)}$$

and the integrals K, L, M, and N will be defined below. Furthermore, the right-hand side of the system [Eqs. (A1)] is defined as

$$\begin{aligned}H^m_l=&\sqrt{4\pi}\left[\frac{b_0}{R}-E_0t_r\frac{\varepsilon_1-\varepsilon_2}{\varepsilon_2}\cos\theta_0\right]\delta_{0l}\delta_{0m}\\&+\sqrt{\frac{4\pi}{3}}E_0\cos\theta_0\delta_{0m}\\&\times\left[\frac{\varepsilon_1}{\varepsilon_2}\delta_{1l}+\frac{\varepsilon_1-\varepsilon_2}{\varepsilon_2}\{\sqrt{3}t_r\zeta^0_{l0}Q^0_{l0}(t_r)-\zeta^0_{l1}Q^0_{l1}(t_r)\}\right]\\&-\sqrt{\frac{2\pi}{3}}E_0\sin\theta_0\delta_{l1}[e^{-i\phi_0}\delta_{1m}-e^{i\phi_0}\delta_{-1m}] \quad \text{(A4a)}\end{aligned}$$

and

$$\begin{aligned}J^m_l=&\sqrt{\frac{4\pi}{3}}E_0\varepsilon_1\cos\theta_0\delta_{0m}\delta_{1l}\\&-\sqrt{\frac{2\pi}{3}}E_0\varepsilon_2\sin\theta_0\delta_{1l}[e^{-i\phi_0}\delta_{1m}-e^{i\phi_0}\delta_{-1m}]\\&-\sqrt{\frac{2\pi}{3}}[(\varepsilon_1-\varepsilon_2)E_0\sin\theta_0][e^{-i\phi_0}\zeta^1_{1l}Q^1_{l1}(t_r)\delta_{1m}\\&-e^{i\phi_0}\zeta^{-1}_{l1}Q^{-1}_{l1}(t_r)\delta_{-1m}]. \quad \text{(A4b)}\end{aligned}$$

The above equations depend on several types of integrals. They are defined as

$$Q^m_{ll'}(t_r)=\int_{-1}^{t_r}dxP^m_l(x)P^m_{l'}(x), \quad \text{(A5a)}$$

$$K^m_{ll'}[\eta](t_r)=\int_{-1}^{t_r}dxP^m_l(x)P^m_{l'}\left(\frac{x-\eta(t_r)}{\sqrt{\chi[\eta](x,1)}}\right)\times\{\chi[\eta](x,1)\}^{-l'-1/2}, \quad \text{(A5b)}$$

$$L^m_{ll'}[\eta](t_r)=\int_{-1}^{t_r}dx\left[P^m_l(x)\partial_r\left\{P^m_{l'}\left(\frac{xr-\eta(t_r)}{\sqrt{\chi[\eta](x,r)}}\right)\times\{\chi[\eta](x,r)\}^{-l'-1/2}\right\}\right]\Bigg|_{r=1}, \quad \text{(A5c)}$$

$$M^m_{ll'}[\eta|](t_r)=\int_{-1}^{t_r}dxP^m_l(x)P^m_{l'}\left(\frac{x-\eta(t_r)}{\sqrt{\chi[\eta](x,1)}}\right)\times\{\chi[\eta](x,1)\}^{l'/2}, \quad \text{(A5d)}$$

and

$$N^m_{ll'}[\eta](t_r)=\int_{-1}^{t_r}dx\left[P^m_l(x)\partial_r\left\{P^m_{l'}\left(\frac{xr-\eta(t_r)}{\sqrt{\chi[\eta](x,r)}}\right)\times\{\chi[\eta](x,r)\}^{l'/2}\right\}\right]\Bigg|_{r=1}. \quad \text{(A5e)}$$

All the above integrals, except the Q integral, have a functional dependency on the function $\eta(t_r)$, which is used as a generic case for either $\mu(t_r)$ or $\bar{\mu}(t_r)$, i.e., for the z coordinate of the position of the multipoles or image multipoles in the main coordinate system $\mathcal{S}$ with the origin in the center of the sphere. Moreover, the functional, $\chi[\eta](x,r)$, appearing in Eqs. (A5b)–(A5e), is defined as

$$\chi[\eta](x,r)=r^2-2\eta(t_r)xr+\eta^2(t_r), \quad x=\cos\theta. \quad \text{(A6)}$$

This functional gives the distance to a given point from the location of the multipoles ($\eta=\mu$) or image multipoles ($\eta=\bar{\mu}$) in terms of the coordinates (r,θ,ϕ) of the main coordinate system $\mathcal{S}$. Notice that $\chi[\eta](x,r)$ is independent of the azimuthal angle ϕ. This is, of course, a consequence of the rotational symmetry around the z axis of the considered geometry.

We would like to stress that with Eq. (3.9) and the definition of $\zeta^m_{ll'}$, Eq. (A3), the matrix elements constituting the left-hand side of our linear system [Eqs. (A2)] do not depend on the actual sign of m but only its value, i.e., $C^m_{ll'}=C^{-m}_{ll'}$, with similar expression for the other (left-hand side) matrix elements. For the right-hand side matrix elements, it follows directly from the definitions of these quantities, Eqs. (A4), that they vanish identically for $m\neq 0,\pm 1$ and that they furthermore satisfy the relations $H^1_l\exp(i\phi_0)=-H^{-1}_l\exp(i\phi_0)$ and $J^1_l\exp(i\phi_0)=-J^{-1}_l\exp(i\phi_0)$. This is so because the right-hand side of the linear system stands entirely for the incident field, which is the same in the present case and the one considered in Ref. 22, and therefore is independent of the location of the multipoles. As a consequence, it follows that the multipole coefficients fulfill the relations

$$A_{l1}e^{i\phi_0}=-A_{l-1}e^{-i\phi_0}, \quad \text{(A7)}$$

$$B_{l1}e^{i\phi_0}=-B_{l-1}e^{-i\phi_0}. \quad \text{(A8)}$$

Hence, the independent multipole coefficients are chosen to those corresponding to $m=0,1$. All other coefficients either vanish or can be expressed in terms of these. Furthermore, it can be shown that if the physical system does not contain any free charges, then the equations with $l=0$ are useless. Thus the linear system [Eqs. (A1)] will only be of interest when $l=1,2,3,\ldots$ and $m=0,1$. The above findings look like those found in the Bedeaux-Vlieger model.[22]

We may take the ''Bedeaux-Vlieger'' limit of our results by placing the multipoles in the center of the sphere, i.e.,

$$\mu(t_r)=0, \tag{A9}$$

$$\bar{\mu}(t_r)=2t_r. \tag{A10}$$

Using the notation of Wind and co-workers[22,23] the above introduced integrals then take the form

$$K^m_{ll'}[\mu](t_r)=Q^m_{ll'}(t_r),\ M^m_{ll'}[\mu](t_r)=Q^m_{ll'}(t_r), \tag{A11a}$$

$$K^m_{ll'}[\bar{\mu}](t_r)=S^m_{ll'}(t_r),\ M^m_{ll'}[\bar{\mu}](t_r)=T^m_{ll'}(t_r), \tag{A11b}$$

$$L^m_{ll'}[\mu](t_r)=-(l'+1)Q^m_{ll'}(t_r),\ N^m_{ll'}[\mu](t_r)=l'Q^m_{ll'}(t_r), \tag{A11c}$$

$$L^m_{ll'}[\bar{\mu}](t_r)=\partial_t S^m_{ll'}(t,t_r)\big|_{t=1}, N^m_{ll'}[\bar{\mu}](t_r)=\partial_t T^m_{ll'}(t_r)\big|_{t=1}. \tag{A11d}$$

The $Q^m_{ll'}$ integral, which is independent of the position of the multipoles, is the same in both works. The linear system of Ref. 22, used to determine the multipole expansion coefficients, can now be obtained from our formulas [Eqs. (A1)] by taking advantage of the relations [Eqs. (A11)]. In this limit our formulas for the linear system reduce, as they should, to those presented by Wind and co-workers.[22,23]

In order to evaluate the potentials in the check of the boundary conditions, the constant b_0, appearing in Eq. (3.13a), must be determined. This constant is obtained in the same way as the above matrix elements, but here only terms containing $Y^*_{0,0}(\theta,\phi)$ will contribute. The result is

$$\begin{aligned} b_0=&\sqrt{\frac{R}{3}}E_0\left(\frac{\varepsilon_1}{\varepsilon_2}-1\right)\cos\theta_0\zeta^0_{01}Q^0_{01}(t_r)+RE_0t_r\left(\frac{\varepsilon_1}{\varepsilon_2}-1\right)\cos\theta_0[1-\zeta^0_{00}Q^0_{00}(t_r)]\\ &+\frac{1}{\sqrt{4\pi}}\sum_{l'=1}^{\infty}A_{l'0}R^{-l'-1}\zeta^0_{0l'}\left[K^0_{0l'}[\mu](t_r)+(-1)^{l'}\frac{\varepsilon_1-\varepsilon_2}{\varepsilon_1+\varepsilon_2}K^0_{0l'}[\bar{\mu}](t_r)+\frac{2\varepsilon_1}{\varepsilon_1+\varepsilon_2}\{K^0_{0l'}[\mu](1)-K^0_{0l'}[\mu](t_r)\}\right]\\ &-\frac{1}{\sqrt{4\pi}}\sum_{l'=1}^{\infty}B_{l'0}R^{l'}\zeta^0_{0l'}\left[M^0_{0l'}[\mu](t_r)+(-1)^{l'}\frac{\varepsilon_3-\varepsilon_4}{\varepsilon_3+\varepsilon_4}M^0_{0l'}[\bar{\mu}](t_r)+\frac{2\varepsilon_3}{\varepsilon_3+\varepsilon_4}\{M^0_{0l'}[\mu](1)-M^0_{0l'}[\mu](t_r)\}\right]. \end{aligned} \tag{A12}$$

*Electronic address: Ingve.Simonsen@phys.ntnu.no
†Electronic address: Remi.Lazzari@sgr.saint-gobain.com
‡Electronic address: Jacques.Jupille@sgr.saint-gobain.com
§Electronic address: Stephane.Roux@sgr.saint-gobain.com

[1] G. Renaud, Surf. Sci. Rep. **32**, 1/2 (1998).
[2] D.E. Aspnes and N. Dietz, Appl. Surf. Sci. **130-132**, 367 (1998).
[3] Y. Borensztein, Physica A **207**, 293 (1994).
[4] D. Martin, F. Creuzet, J. Jupille, Y. Borensztein, and P. Gadenne, Surf. Sci. **377-379**, 958 (1997).
[5] D. Martin, J. Jupille, and Y. Borensztein, Surf. Sci. **402-404**, 433 (1998).
[6] D. Martin and J. Jupille (unpublished).
[7] R. Lazzari, J. Jupille, and Y. Borensztein, Appl. Surf. Sci. **142**, 451 (1999).
[8] J.C. Maxwell Garnett, Philos. Trans. R. Soc. London, Ser. A **203**, 385 (1904).
[9] U. Kreibig and M. Vollmer, *Optical Properties of Metal Clusters*, Springer Series in Material Science Vol. 25 (Springer-Verlag, Berlin, 1995).
[10] G. Mie, Ann. Phys. (Leipzig) **25**, 377 (1908).
[11] R. Landauer, in *Proceedings of the First Conference on the Electromagnetic and Optical Properties of Inhomogeneous Media*, edited by J. C. Garland and D. B. Tanner (AIP, New York, 1978).
[12] R.G. Barrera, M. del Castillo-Mussot, G. Monsivais, P. Villaseñor, and W.L. Mochán, Phys. Rev. B **43**, 13 819 (1991).
[13] R.G. Barrera, G. Monsivais, and L. Mochán, Phys. Rev. B **38**, 5371 (1988).
[14] T. Yamaguchi, S. Yoshida, and A. Kinbara, Thin Solid Films **18**, 63 (1973).
[15] T. Yamaguchi, S. Yoshida, and A. Kinbara, Thin Solid Films **21**, 173 (1974).
[16] D. Bedeaux and J. Vlieger, Physica A **67**, 55 (1973).
[17] D. Bedeaux and J. Vlieger, Physica A **73**, 287 (1974).
[18] J. Vlieger and D. Bedeaux, Physica A **82**, 221 (1976).
[19] D. Bedeaux and J. Vlieger, Thin Solid Films **69**, 107 (1980).
[20] J. Vlieger and D. Bedeaux, Thin Solid Films **102**, 265 (1983).
[21] E. Kretschmann, Z. Phys. **227**, 412 (1969).
[22] M.M. Wind, J. Vlieger, and D. Bedeaux, Physica A **141**, 33 (1987).
[23] M.M. Wind, P.A. Bobbert, J. Vlieger, and D. Bedeaux, Physica A **143**, 164 (1987).
[24] J. D. Jackson, *Classical Electrodynamics* (Wiley, New York, 1975).
[25] M.M. Wind, P.A. Bobbert, and J. Vlieger, Thin Solid Films **164**, 57 (1988).
[26] F. Didier and J. Jupille, J. Adhes. **58**, 253 (1996).
[27] M.T. Haarmans and D. Bedeaux, Thin Solid Films **224**, 117 (1993).
[28] E.D. Palik, *Handbook of Optical Constants of Solids* (Academic Press, New York, 1985).
[29] P. M. Morse and H. Feshbach, *Methods of Theoretical Physics* (McGraw-Hill, New York, 1953), Pts. 1 and 2.